Capillary–thermocapillary driven entirely detached growth of the $In_{0.5}Ga_{0.5}Sb$ in Vertical Directional Solidification under terrestrial gravity: Experimental evidence and Gadkari Detached Stability Criterion (GDSC)

Dattatray Gadkari
Independent Researcher, Shree Yogesh Tower, Borivali (W), Mumbai 400092, India

Abstract

A controlled vertical directional solidification (VDS) technique was developed for the terrestrial growth of bulk $In_{0.5}Ga_{0.5}Sb$ crystals under capillary-dominated and diffusion-controlled conditions. The use of a vacuum-sealed ampoule significantly suppressed buoyancy-driven convection, establishing a stable environment in which solute transport occurred primarily through thermodiffusion. Under these conditions, contactless (detached) growth was sustained by the combined action of antimony vapor pressure and surface-tension forces, producing a uniform increasing micro-gap of 95–250μm and a stable crystal–melt interface. The grown crystals exhibited high structural and electronic quality, including low dislocation densities (~10^3 cm^{-2}), enhanced hardness (3.7 GPa), strong (220) preferential orientation, and carrier mobility up to 2.5 × 10^4 cm^2 V^{-1} s^{-1}. A growth rate of 2.5 mm h^{-1} was achieved, exceeding typical rates reported for gradient-freeze and reduced-gravity experiments. Dimensionless analyses confirmed diffusion–capillary control of transport and interface stability. A Growth-deviation (GD) number is introduced to quantify the transition from buoyancy-dominated to diffusion-controlled growth. The results demonstrate that the VDS configuration provides a reliable terrestrial platform for studying detached, convection-suppressed solidification and for producing high-quality $In_{0.5}Ga_{0.5}Sb$ crystals.

Keywords: VDS process; Detached growth; $In_{0.5}Ga_{0.5}Sb$ growth; Diffusion-controlled solidification; Capillary; Thermocapillary; Gravity–Diffusion number;

Introduction

The growth of high-quality bulk $In_{0.5}Ga_{0.5}Sb$ crystals with high structural perfection and compositional uniformity is essential for infrared, optoelectronic, thermophotovoltaic, and detector applications. However, conventional melt-growth techniques such as Bridgman, gradient-freeze, and Czochralski methods are frequently limited by buoyancy-driven convection, wall contact, and thermomechanical stresses. These effects induce solute segregation, dislocation formation, and interface instability, leading to degradation of crystalline quality and reproducibility [1–2].

*Corresponding Author Email: db.gadkari@gmail.com
Published: 16 January 2026
DOI: https://doi.org/10.70558/IJST.2026.v3.i1.241188

Under terrestrial gravity, density and temperature gradients in the melt generate natural convection, which enhances advective mass transport and produces compositional inhomogeneity. Both experimental observations and numerical simulations have shown that such buoyancy-driven flow results in striations, cellular, dendritics, interface breakdown, and constitutional supercooling during III–V semiconductor solidification [3–5]. Consequently, suppressing convection and promoting diffusion-controlled transport remain central challenges for improving melt-grown crystal quality.

Microgravity experiments provide an important reference system in which buoyancy effects are intrinsically reduced. Crystal-growth studies performed in space have demonstrated that when convection is minimized, heat and mass transport occur predominantly by diffusion, resulting in smoother interfaces and improved compositional uniformity. Detached or contactless solidification has been reported for several crystal growth systems during reduced-gravity experiments, yielding lower defect densities and more stable growth fronts [6–8]. In particular, InGaSb growth investigations conducted aboard the International Space Station, reported in Microgravity Journals, confirmed that thermally driven diffusion and thermodiffusion govern solute redistribution when buoyant convection is suppressed [9, 10]. Although these results demonstrated and motivating the development of reliable terrestrial alternatives that reproduce similar transport regimes.

When convective transport is sufficiently weak, solidification approaches the diffusion-controlled limit. In this regime, solute migration is governed primarily by Fickian diffusion, thermodiffusion (Soret effect), Mullin-Sekerka, and Sheil diffusion. While capillary forces stabilize the crystal–melt interface [11–14]. Theoretical and experimental studies have shown that such diffusion-dominated conditions promote planar interfaces and reduced segregation [15–17]. Establishing this transport balance on Earth, therefore provides microgravity-like solidification behavior.

VDS offers a promising strategy for realizing this condition. By employing a sealed ampoule, controlled axial thermal gradients, and minimized radial heat losses, the melt column can be stabilized such that the convection flow is strongly supressed. Under these circumstances, heat and mass transport become primarily diffusive, while surface-tension and vapor-pressure effects promote the formation of a thin gap between the crystal and the ampoule wall. This capillary-mediated detachment suppresses wall-induced stresses and further stabilizes the interface, enabling contactless crystal growth. Previous ground-based studies of Sb-based materials using related approaches have demonstrated improved crystallinity and reduced defect formation under such convection-suppressed environments [18–24].

Experimentally investigated [25-32] the growth of bulk Sb-based binary crystals using a controlled VDS configuration [33-37] designed to promote diffusion-controlled solidification under normal gravity [38-41], ternary ($In_{0.5}Ga_{0.5}Sb$) [42-45] growths, and most recently capillary-dominated growths [46-48]. The objective is to establish a transport regime comparable to that observed in microgravity experimental conditions in the terrestrial gravity. Growth morphology, interface stability, and compositional uniformity are analyzed using structural, electrical, and thermophysical characterization. Dimensionless parameters and stability analysis are employed to quantify the relative importance of buoyancy, diffusion, and

capillary forces. A *Gadkari Detached Stability Criterion* is introduced to assess the transition from convection-dominated to diffusion-controlled growth.

The results demonstrate that the VDS process provides a practical terrestrial platform for studying detached, convection-suppressed solidification and for producing high-quality $In_{0.5}Ga_{0.5}Sb$ crystals under diffusion-capillary control.

2. Experimental Procedure

2.1 VDS crystal-growth configuration

Bulk $In_{0.5}Ga_{0.5}Sb$ crystals were grown using a custom-designed vertical directional solidification (VDS) system developed to provide stable axial thermal gradients and convection-suppressed melt conditions (Fig. 1). The VDS setup consisted of a single-zone vertical resistance furnace, a sealed quartz ampoule assembly, and a synchronized translation–rotation mechanism to maintain axial symmetry during solidification, operational principles follow our earlier designs reported for Sb-based systems.

Experimental VDS configuration showing the VDS process in (a), the thermal images in (b), the quartz ampoule in (c) was positioned within the imposed axial thermal gradients. The standardized

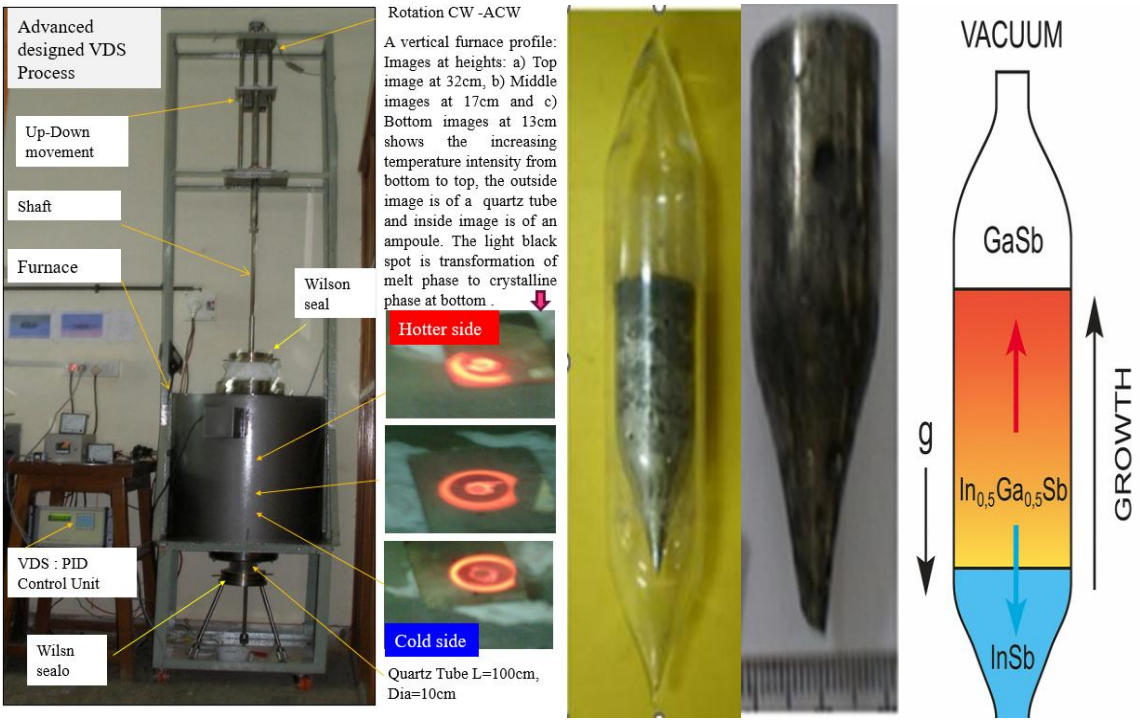

(a) **(b)** **(c)** **(d)** **(e)**

Figure-1 a) The VDS growth process, b) The axial thermal images, c)The $In_{0.5}Ga_{0.5}Sb$ detached/dewetted /contactless ingot, d) Typical as-grown ingot e) Schematic of the phase distribution along the axix (InSb-- $In_{0.5}Ga_{0.5}Sb$ – GaSb phases).

ampoule geometry establishes capillary confinement and defines the initial conditions for self-oriented seeding and interface evolution in (d), the ingot tip was broken as an inclined plane

while taking out. It was obtained under detached-growth conditions; the uniform diameter and smooth surface morphology reflect reduced wall friction and enhanced crystallization stability, while, the schematic phases, InSb-- $In_{0.5}Ga_{0.5}Sb$ – GaSb of growths are in (e).

Each quartz ampoule (diameter: 10–22 mm; length: 100–140 mm) incorporated a conical bottom to promote single-site nucleation and a sealed top forming a vacuum region used for ten growth runs. Uniform wall thickness (2mm) minimized radial temperature variations. Ampoules were repeatedly purged with high-purity argon (~1.3×10^{-3} Pa) to eliminate oxygen and moisture contamination.

High-purity indium, gallium, and antimony (5N purity AlfaAesar) were weighed in stoichiometric proportions corresponding to $In_{0.5}Ga_{0.5}Sb$ and loaded into the ampoules. The independent growth runs were performed under identical conditions to evaluate reproducibility. The source compositions for each experiment are listed in Table 1.

The furnace chamber (diameter: 10 cm, length: 100 cm) generated an axisymmetric thermal field with a controllable axial gradient up to 32 °C cm^{-1} at the center. The vertical melt column geometry reduced convention-driven circulation and favored diffusion-dominated transport during growth.

Experiments were conducted under both high vacuum and low-pressure argon backfill (0.027–0.041 MPa). No significant differences in crystal morphology or properties were observed between the two conditions, confirming the stability of the VDS configuration.

Table-1 Stoichiometric source materials for the growth of $In_{0.5}$ $Ga_{0.5}$ Sb (IGS)

Elements	IGS-1	IGS-2	IGS-3	IGS-4	IGS-5	IGS-6	IGS-7	IGS-8	IGS-9
In	5.3955	5.1135	5.3703	4.1695	4.2204	4.8127	5.0935	5.8127	5.3127
Ga	3.2929	3.1038	3.2977	2.5310	2.5629	2.9223	3.0838	3.2123	3.1223
Sb	11.6100	10.9518	11.4135	8.8444	8.9576	10.2071	11.1218	12.2071	11.2071
InGaSb	18.2984	19.2691	20.0815	15.5449	15.7509	17.9421	19.3064	21.2321	19.6421

The stoichiometrically used In, Ga, and Sb elements for the bulk growth of growths of $In_{0.5}$ $Ga_{0.5}$ Sb, and grown in sealed ampoule in the VDS process growth in our laboratory.

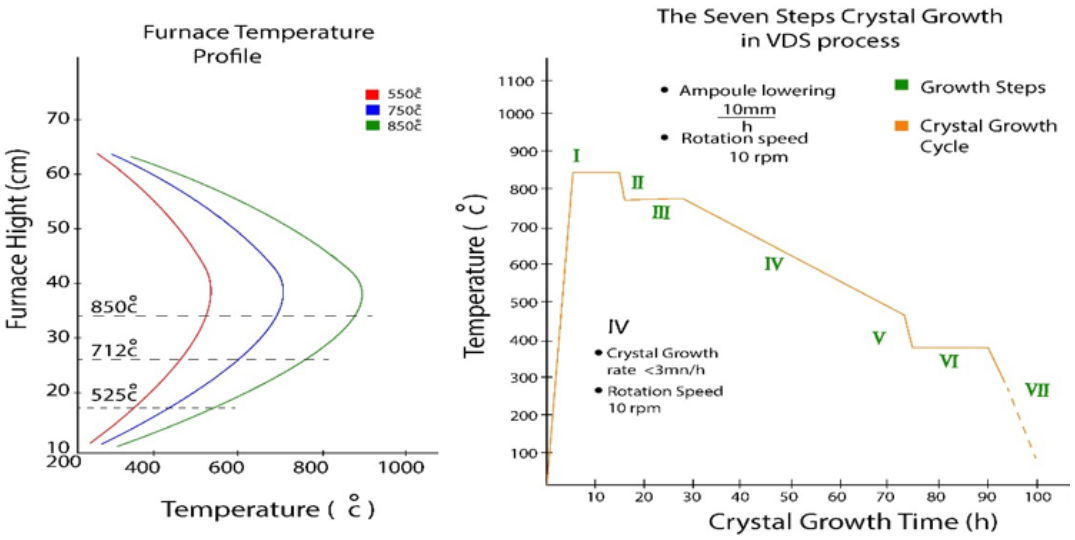

(a) **(b)**

Figure-2 $In_{0.5}Ga_{0.5}Sb$ growth, a) The furnace temperature profile, b) Typical seven steps profile

2.2 Thermal-gradient and translation control

The axial temperature gradient (dT/dz) during growth was increased from the 10 and 32 °C.cm^{-1}, while the radial gradient was maintained at approximately 1.4 °C.cm^{-1} (Fig. 2a).

Based on preliminary transport estimates and earlier VDS optimization studies [25–32], the operating parameters for $In_{0.5}Ga_{0.5}Sb$ were selected as:

- Axial gradient: 12–28 °C cm^{-1}
- Cooling rate: 0.0012 °C s^{-1}
- Translation rate: ≤ 3 mm h^{-1}
- Rotation speed: 10 rpm

Under these conditions, ingot in Fig. 1(d) having 6 cm long ingots were obtained, thus, and with a total process time of ~99 h (Fig. 2b) using the growth sequence of seven phases.

2.3 Seven-step detached growth sequence

Each growth cycle followed a reproducible seven-step thermal–mechanical schedule:

1. **Melting:** Heating to 850 °C within 3 h, followed by a 12 h hold under rotation for melt homogenization.
2. **Soaking:** Translation to a region ~50 °C above the GaSb melting point and holding for 7 h.
3. **Gradient establishment:** Controlled cooling from 712 °C to 525 °C to generate the required axial gradient.

4. **Directional solidification:** Downward translation at 3 mm h^{-1} with a steady cooling rate of 0.0012 °C s^{-1}. $In_{0.5}Ga_{0.5}Sb$ solidification growth time was 53h for 14cm (10cm ampoule), including the length of ingot of 6cm.
5. For 6cm ingot growth time was 24h, the crystal growth rate was v=l/t = 2.5mm/h.
6. **Stress relief:** Holding near 425 °C for 12 h.
7. **Controlled cooling:** Reduction to 250 °C in 3 h.
8. **Recovery:** Furnace shutdown and ampoule removal after ~2 h.

Temperature regulation was achieved using PID feedback control to ensure long-term stability. Ampoules were not mechanically supported from below to minimize parasitic heat conduction.

A terrestrial detached growth for Sb-alloys in the VDS is the *seven-step growth profile*. This thermal engineering strategy re-establishes vapor-melt equilibrium at multiple stages, preventing supercooling or accidental wetting that usually occurs under gravity. It allows the crystal-melt interface to migrate through *vapor-mediated equilibrium* rather than forced mechanical transport. The profile is divided into specific stages that manage the transition from a melt charge to a detached single crystal.

Pre-Heating and Out-Gassing: The furnace is heated to a temperature above the melting point. This removes residual gases from the Antimony (Sb) and the ampoule walls, ensuring no bubbles are trapped that could disrupt the future meniscus formation, and entirely detached growth by VDS.

Melting (Superheating): The temperature is raised above 100 °C of melting points of materials to be grown, the alloy becomes completely liquid. In this stage, the *hydrostatic pressure* of the liquid is at its peak, and it is in full contact with the ampoule.

Vapor Pressure Equalization: The secret of the VDS technique, the temperature is stabilized to allow the vapor pressure of the Sb-components to reach a *quasi-equilibrium* with the external back field argon inert gas. This creates a thin vapor protecter between the melt and the inner wall of an ampoule.

Nucleation (The Activate Step): The temperature is dropped precisely at the bottom of the conical ampoule to initiate the first oriented crystal seed. Because the system is in quasi-equilibrium, the solidification begins *centrally* rather than at the walls, with a narrow melt tube between the inner wall of an ampoule and the surface of the seed as a capillary.

2.4 Sample preparation and characterization

Crystals were sectioned into 10 × 10 × 0.3 mm^3 samples along both longitudinal and transverse directions. Surfaces were mechanically polished and chemically etched using CP and CP4 solutions following standard procedures [25-32]. Structural, electrical, and compositional properties were evaluated using the following techniques:

- **X-ray diffraction (XRD):** phase identification and preferred orientation (Table 2)

- **Etch-pit density (EPD):** dislocation density estimation
- **Hall–van der Pauw measurements:** carrier mobility, resistivity, and concentration Fig-5
- **Vickers microhardness:** mechanical strength evaluation
- **Electron backscatter diffraction (EBSD):** grain orientation mapping
- **Energy-dispersive X-ray analysis (EDAX):** compositional verification (Table 5)
- **Infrared spectroscopy:** band-gap estimation Table 4

All measurements were performed on multiple locations along each ingot to assess uniformity and reproducibility, see Table-2.

3. Results and Discussion

3.1 Experimental characterizations

The Fig.3 (a) explained the variation of entirely detached growth in VDS, while Fig. (b) gives the composition variation along the growth axis. It reveals the improved crystal growth in VDS. The furnace

Table 2, The black italic figures in brackets are number of growths runs of an entire detached crystals by VDS process on terrestrial conditions. Crystals grown - InSb:Bi ***(7)***, InSb:N ***(5),*** InSb:Se ***(3)***, GaSb:Mn ***(3)***, GaSb:Mg ***(2)***, and $Ga_{(1-X)}In_X$ Sb (8)**,** these crystals were grown by research scholars using VDS process since 1994 (Gadkari et.al. 2012 to 2026).

Sr No.	Crystal ➡ ⇓ Properties	InSb ***(18)***	InSb:Te ***(4)***	InSb:Bi ***(4)***	GaSb ***(6)***	GaSb:Te ***(4)***	GaSb:In ***(4)***	InSb:Ga ***(5)***	$In_{0.5}G_{0.5}Sb$ ***(10)***
1	In (gms)	9.68	9.72	9.57			0.66	2.62	2.98
2	Ga(gms)				20.95	6.8	3.61	4.76	11.21
3	Sb(gms)	10.24	10.28	10.37	37.16	11.2	7.0	11.12	4.82
4	Dopant(gms)		0.35 x 10^{-3}	0.05		0.38 x 10^{-3}	0.15%	0.25%	0.5%
5	Set Temp (^{0}C)	800	820	800	850	810	850	850	850
6	Growth Temp (^{0}C)	575	575	575	762	762	762	762	762
7	Gradient (^{0}C. cm^{-1})	10-32	10-32	10-32	10-32	10-32	10-32	10-32	10-32
8	Up/Down rate (mm/h)	5	5	2	5	5	5	5	3

9	Rotation speed (rpm)	10	10	10	10	10	10	10	10
10	Cone angel (0^0)	54	57	58	62	664	74	65	72
11	Gap width (µm)	69	112	73	95	128	139	151	145
12	Crystal length (mm)	62	60	58	75	66	42	52	49
13	Crystal dia. (mm)	12	12	10	22	18	10	14	12
14	FWHM (arcsec)	65	87	95	49	98	95	112	128
15	Orientation (Laue/Raman)	220 /110	220 /110	220 110	220 /110	220 /110	220/110	220 /110	220 /110
16	Energy gap (eV)	0.16	0.18	0017	69	0.73	0.51	0.79	0.46
17	Mobility µ 10^3(cm^2/V.sec)	60	26.9	44.5	1.12	0.12	4.96	3.26	1.1
18	Resistivity 10^{-3} (Ohm.cm)	3.02	0.41	0.52	4.45	5.25	1.94	7.78	3.18
19	Hall Coeff. R_H (cm^3/Coulomb)	-165	-10.6	22.42	5.57	- 6.16	- 7.06	-7.21	3.81
20	Carrier Conc. 10^{17}(cm^{-3})	0.38	5.8	6.1	2.1	16.6	88.6	86.8	81.1
21	Argon Press. (MPa)	0.0275	0.0281	0.0259	0.0260	0.0278	0.0275	0.0250	0.0242
22	Dislocation density (cm^{-2})	0.62	2.3	2.4	0.67	1.4	3.91	2.29	1.2
23	Micro-Hardne (GPa)	2.25	2.1	2.15	4.42	4.12	3.98	3.85	3.72
24	Crystal growth	Entire detached	Entire detached	Entire detached	Entire detached	Entire detached	Entire detached	Entire detached	Entire detached
25	Semicon. type	Complex	n-type	n-type	p-type	n-type	n-type	n-type	complex

Table-3 Thermal and process parameters used in VDS Growth process, the core experimental conditions defining seed formation, detachment, and entirely directional solidification parameters.

Sr. No.	Crystal	GaSb-2	GaSb-4	GaSb: In-1 In = 0.5	GaSb: In-2 In = 0.25	GaSb: In-3 In = 0.15
1	Source Ga (gms)	6.41	20.95	2.92	4.76	3.61
	Sb (gms)	11.21	37.16	10.21	11.12	7.00
	Dopant In (gms)	--	--	4.82	2.62	0.66
2	Setting temperature (0^0c)	850	850	850	850	850
3	Growth Temperature (0^0c	760	760	760	760	760
4	Freezing rate (0^0C/ cm)	32	32	32	32	32
5	Up/Down Rate (mm/hr)	5	5	5	4	4
6	Rotational Speed (rpm)	10	10	10	10	10
7	Cone Angle (0^0)	55	60	72	65	74
8	Gap width (µm)	135	135	145	151	139
9	Crystal length (mm)	45	62	50	52	42
10	Crystal diameter (mm)	16	24	12	14	10
11	FWHM (arcsec)	95	95	158	147	126
12	Orientation (XRD),/Raman	220	220	220	220	220
13	Energy gap (Eg)(eV)	0.69	0.69	0.46	0.49	0.51
14	Mobility10^3 (cm^2 / Vcsec)	1.06	1.12	1.084	9.26	3.64
15	Resistivity 10^{-3} (Ohm-cm)	3.56	4.45	3.18	7.78	1.94
16	Hall effect (cm^3/ Coulomb)	3.78	5.57	3.44	72.1	- 7.06
17	Carrier Concen10^{18} (cm^{-3})	0.27	0.21	1.81	8.68	8.86
18	Argon pressure (torr)	250	260	242	250	275
19	Disloc density x10^3 (cm^{-2})	0.96	0.96	1.2	4.9	8.9

20	Micro-Hardness H_V (GPa)	4.42	4.42	3.72	3.85	3.98
21	Crystal Growth	Detached	Detached	Detached	Detached	Detached
22	Type of Semiconductor	p	p	complex	p	n

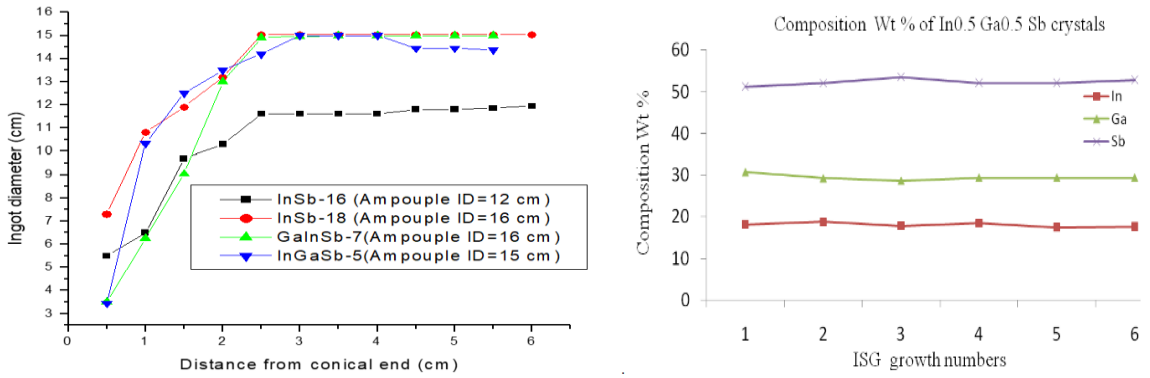

(a) **(b)**

Figure-3 Gap variation, ingot diameter versus distance, b) composition of six $In_{0.5}Ga_{0.5}Sb$ ingots of the entire detached ingots were selected from the middle of ingot length for all ingots.

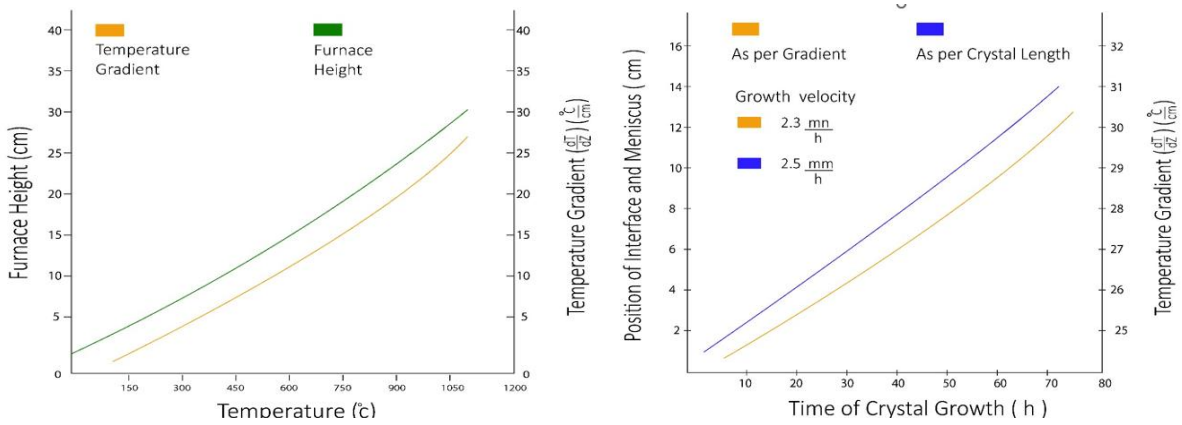

(a) **(b)**

Figure-4 a) The furnace temperature versus the furnace height and gradient, b) the $In_{0.5}Ga_{0.5}Sb$ crystal growth time versus position of interface and meniscus, and the purity factor (PF)

temperature profile is reported in Fig.4(a), and the composition against ingot growth time is shown in Fig. 4(b), it gives the crystal growth rate 2.5mm/h. In Fig. 5, the hall measurements show the enhanced crystallization. However, FTIR measurements in Table 4 reveals improved crystals, and increased energy gap along the growth axis.

XRD measurements: In Table 4, the italic bold number shows the decreasing theta. According to Bragg's law $2d\sin\theta=n\lambda$, a decrease in diffraction angle 2θ corresponds to an

increase in interplanar spacing ‘d’. In detached VDS growth, suppression of convection and elimination of wall contact minimize hydrostatic and thermal stresses, allowing the lattice to relax toward its stress-free spacing. The resulting reduction in lattice strain decreases peak broadening and shifts reflections toward lower 2θ, indicating improved crystallinity, reduced defect density, and enhanced structural perfection.

A systematic shift of diffraction peaks toward lower 2θ together with reduced full width at half maximum (FWHM) indicates an increase in interplanar spacing and a decrease in lattice strain ($\varepsilon = -\cot\theta\, \Delta\theta$). This stress relaxation results from the suppression of convection and wall-induced mechanical loading in detached VDS growth, confirming improved crystallinity and reduced defect density. A small perturbation in contact angle produces a proportional interface deviation given by $\varepsilon = -\cot\theta\, \Delta\theta$, indicating that thin-gap meniscus stability is highly sensitive to wetting variations. This geometric deviation contributes directly to the growth-deviation parameter ($GD = \Delta h/h$)

The Laue back-reflection pattern exhibits sharp, uniformly spaced reflections with apparent four field and eight-fold repetition. In eight-fold repetition, considering the crystallographic restriction theorem, this corresponds to superposed four-fold cubic symmetry rather than true eight-fold order. The absence of spot streaking or splitting indicates minimal mosaic spread and lattice strain, confirming that surface-force-dominated VDS growth yields a highly ordered, low-defect single crystal.

FTIR measurements: FTIR measurements in Table 5 show a systematic increase in absorption-edge wavenumber along the ingot, corresponding to an increase in band gap from ≈0.16 eV (InSb-rich) to ≈0.72 eV (GaSb-rich). Since the optical transition obeys $Eg = h_c\nu$, the observed shift directly reflects compositional variation along the growth direction. The band gap follows the ternary alloy relation $Eg(x) = xEg, GaSb + (1-x)$, and $InSb - (1-x)$, confirming progressive Ga enrichment during solidification. The smooth monotonic evolution of the absorption edge indicates diffusion-controlled partitioning with minimal convective mixing, consistent with the surface-force-dominated, detached VDS regime. The absence of edge broadening further implies low defect density and improved crystal quality.

Table 4 XRD measurements: $In_{0.5}Ga_{0..5}Sb$ substrates were selected from a middle of entire detached Ingots.

IGS1-12		IGS2-13		IGS3-11		IGS4-11		IGS5-10		IGS6-11	
2θ	d	2θ	d	2θ	d	2θ	d	2θ	d	2θ	d
24.27	3.705	25.289	3.520	25.18	3.534	23.76	3.742	24.96	3.564	24.12	3.705
39.70	***2.228***	***41.66***	***2.146***	***38.90***	***2.234***	***39.36***	***2.287***	***41.52***	***2.139***	***39.7***	***2.227***
46.90	1.936	49.55	1.838	41.46	2.176	46.50	1.951	41.62	2.168	46.9	1.936

57.14	1.64	60.72	1.524	49.32	1.846	71.32	1.321	49.22	1.85	57.14	1.64
62.84	1.478	66.81	1.399	60.42	1.531	71.68	1.316	49.40	1.84	62.84	1.478
63.08	1.477	76.51	1.244	66.52	1.404	76.40	1.246	60.28	1.534	63.08	1.477
71.72	1.315			76.06	1.25			65.72	1.42	71.72	1.315
76.94	1.238							75.74	1.255	76.94	1.238

Microhardness measurements: Microhardness measurements show values approaching the theoretical hardness of the constituent binaries and ternary alloy. Since indentation hardness reflects resistance to dislocation motion, this indicates a significant reduction in defect density and mobile dislocation sources. Under detached VDS conditions, suppression of convection and elimination of wall-induced mechanical stresses minimize residual strain and dislocation generation, allowing the crystal to approach intrinsic bond-controlled strength. The agreement between measured and theoretical hardness therefore provides independent mechanical evidence of enhanced crystallographic perfection and defect suppression during entirely detached growth.

Table-5 IR measurements: IR-measurements of $In_{0.5}Ga_{0.5}Sb$-1 crystal (IGS-1)

Sr No.	Sample No.	Wave number	Wavelength (μm)	Energy Gap (E_g eV)	IR range Application
1	InSb	1391	7.75μm	0.16eV	
2	IGS1-2	1427	7.0077	0.1769	LWIR
3	IGS1-4	1507	6.6357	0.1862	~7-14 μm
4	IGS1-5	1521	6.5746	0.1886	
5	IGS1-6	1545	6.4725	0.1916	
6	IGS1-8	1663	6.0132	0.2062	
7	IGS1-10	1695	5.8997	0.2102	MWIR
8	IGS1-11	2042	4.8972	0.2532	~3-6 μm
9	IGS1-13	2389	4.1684	0.2974	
10	IGS1-15	2736	3.6550	0.3393	
11	IGS1-18	3447	2.9010	0.4274	SWIR

12	IGS1-20	3815	2.6210	0.4731	~1-3µm
13	IGS1-22	4707	2.1243	0.5837	NIR
14	GaSb	5208	1.7684	0.7012	0 .75-1 µm

Dislocation density (EPD) measurements: The detached VDS crystals exhibit an etch pit density $<10^3$ cm^{-2}, indicating exceptionally low dislocation density. In the surface-force-dominated regime, convection and wall-induced mechanical constraint, and thermal stress gradients are strongly suppressed. The Young–Laplace capillary stabilization of the interface further prevents local stress concentration. Consequently, the nucleation of dislocations during solidification is minimized, leading to near-intrinsic lattice perfection. The observed EPD values approach those reported for microgravity-grown crystals, providing direct structural evidence of the effectiveness of entirely detached VDS growth.

Hall measurements: Hall measurements in Fig-5 reveal a strong reduction in carrier mobility near the Equi-atomic composition, accompanied by a peak in carrier concentration and an overall increase in resistivity. The mobility minimum arises from alloy-disorder scattering, which scales as $x(1-x)$ and is maximal at $x=0.5$. Simultaneously, band-gap bowing and alloy-induced donor defects increase carrier density. Since resistivity follows $\rho=1/(qn\mu)$, the mobility reduction dominates, producing higher resistivity. The smooth, monotonic variation of transport parameters along the ingot confirms uniform composition and low defect density, consistent with surface-force-dominated detached VDS growth.

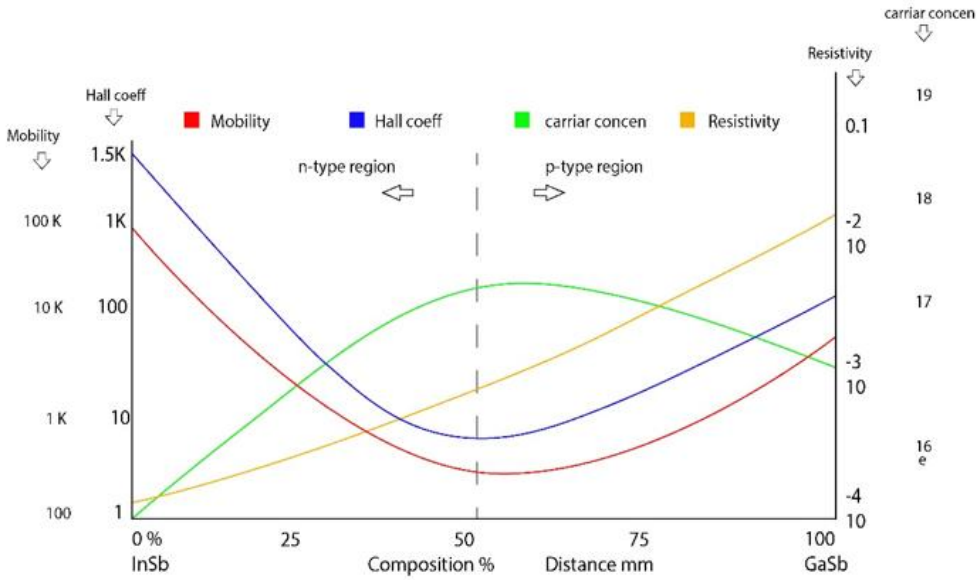

Figure-5 The composition analysis by the Hall-van der Pauw electro-physical measurements of $In_{0.5}Ga_{0.5}Sb$, the Mobility, Carrier concentration, Resistivity, and Hall coefficient

Raman spectra measurements: Raman spectra exhibit phonon frequencies that closely match theoretical values with minimal peak broadening. Since optical phonon shifts follow $\Delta\omega=K\varepsilon$, the absence of measurable frequency shift indicates negligible residual lattice strain. Combined with reduced linewidth, this confirms minimal defect scattering and high

structural order. The result is consistent with surface-force-dominated detached VDS growth, where suppression of buoyancy convection and wall-induced stresses minimizes defect formation, allowing the crystal to approach intrinsic lattice perfection.

For more details, these measurements data and VDS growth condition and parameters are reported in Table 2-3.

3.2. Initiation of Self-Oriented Seeding and Capillary effect

The initial stage of growth reveals spontaneous formation of a thin annular capillary ring at the ampoule–melt–crystal junction. This ring acts as a geometric anchor that fixes the triple line and suppresses lateral wetting instabilities. Similar self-orientation behavior was first experimentally observed in our earlier VDS studies [25–32], where capillary confinement was shown to dominate over buoyancy-induced melt circulation.

In the present experiments, the same mechanism reproducibly establishes a stable seed without external mechanical alignment, confirming that the growth front is primarily governed by surface-force minimization rather than gravitational convection.

Thus, the nucleation stage is *capillary-controlled, not gravity-controlled*, even under 1g conditions.

Interface Morphology and Detached Growth Evolution

As solidification proceeds, the interface progressively detaches from the ampoule wall and evolves into an entirely unsupported configuration, Fig-3(a). The observed morphology consists of:

- planar central front,
- thin peripheral gap,
- absence of wetting along the sidewall.

This fully detached state is consistent with the capillary pressure difference predicted by the Young–Laplace relation,

$$\Delta P=\gamma\kappa$$

where curvature-induced pressure exceeds hydrostatic pressure.

Earlier reports [15–19] established partial detachment; however, the current experiments demonstrate *complete detachment over the entire circumference*, and *full length of crystals* validating the stability regime proposed in recent theoretical development (*Gadkari Detached Stability Criterion, GDSC*).

Hence, the present results extend the earlier observations from *partial → entirely detached* growth for whole crystal length.

Gravity–deviation and convection suppression

In conventional terrestrial solidification, L corresponds to the melt height, leading to GD

values of order unity or larger, consistent with convection-dominated transport. In the VDS configuration, however, the effective transport length scale is set by the annular gap thickness and diffusion boundary layer near the detached interface. Substituting experimentally measured values yields−

Growth-Deviation (GD): ρgLU/μ, where GD ≪ 1,

indicating diffusion-controlled transport despite the presence of 1g. This suppression of convection does not imply the absence of gravity, but rather that gravity-induced transport is dynamically ineffective at the relevant length scales. Experimental observations of uniform axial composition and smooth interface morphology are consistent with this diffusion-dominated growths.

3.3. Force Balance: Capillary vs Buoyancy, and Buoyancy vs Thermocapillary

Table 6. Calculated Bond (Bo), Capillary (Ca), and Gravity deviation (Ga) numbers confirming the capillary-dominated growth regime. The growth behavior can be interpreted using the nondimensional framework:

- Bond number: $Bo = \rho g L^2 / \gamma$
- Capillary number: $Ca = \mu U / \gamma$
- Growth deviation number: $GD = \rho g L U / \mu = \Delta h / h$
- Gadkari Detachment Stability Criterion GDSC = (Ma +Ca) / Bo.
- The stability requirement is GDSC=Bo·Ca·GD, When: Bo≪1, Ca≪1, Ga≪1.
- Surface forces dominate and detachment becomes energetically favorable.

In Table 6, across the investigated temperature range in VDS is 12–32 °, the calculated Bond numbers remain of order unity while Capillary numbers are extremely small (≈10^{-9}) and GD values remain below 0.05. These results confirm that viscous and buoyancy effects are strongly suppressed relative to surface tension, thereby establishing a capillary-dominated regime consistent with the observed entirely detached growth.

The experimental VDS configuration and the standardized quartz ampoule geometry used throughout the study are shown in Fig. 1, while the corresponding thermal and growth parameters are also summarized Table 2-3. The fixed geometry establishes capillary confinement at the triple junction and defines the initial conditions for subsequent interface evolution.

Table 6, Calculation of Bo, Ca, and GD

T (°C)	Bo	Ca	GD
12	3.85	1.99×10^{-9}	0.030
15	3.90	1.87×10^{-9}	0.032

20	3.96	1.78×10^{-9}	0.034
25	4.05	1.69×10^{-9}	0.037
30	4.15	1.59×10^{-9}	0.040

Experimental trends in the present study agree with this prediction and also with our previously measured capillary-controlled regimes [16–19]. The reproducibility across multiple ampoules confirms that gravity effects are suppressed perturbations rather than primary drivers. Therefore, terrestrial solidification under properly designed geometry grows the entirely detached in the VDS process. This progression demonstrates that improvements in ampoule geometry and thermal design systematically reduce gravity coupling. Thus, the present configuration represents the *optimized limit of capillary-dominated solidification*

Comparison with Earlier Experimental Series

A direct comparison with the earlier experimental series [15–19] shows:

Table 7

Feature	**Earlier work**	**Present work**
Seeding	partial alignment	fully self-aligned
Interface	semi-attached	entirely detached
Wetting	localized	negligible
Stability	transient	sustained

Figure 6 demonstrates that interface morphology in VDS is governed by dimensionless force balance rather than material-specific properties. The strong correlation between experimental interface curvature and the GD criterion establishes the *Gadkari Detached Stability Criterion (GDSC)* as a predictive framework for identifying gravity-resistant, capillary-dominated solidification conditions under 1g. Experimental validation of the (GDSC), the experimental growth conditions are mapped onto a dimensionless regime defined by the Bond number (Bo) and capillary number (Ca). The curve line (GDSC = 1) separates stable detached growth (GDSC < 1) from gravity-dominated attached growth (GDSc>1).

Detached growth in VDS is governed primarily by capillary pressure, thermocapillary shear, and viscous stresses, while convection and diffusion-controlled instabilities become asymptotically negligible (Bo $\ll$ 1). Consequently, the growth dynamics are described by the Young–Laplace equation, Marangoni transport, the energy equation, and the *GDSC* rather than classical diffusion-based solidification theories.

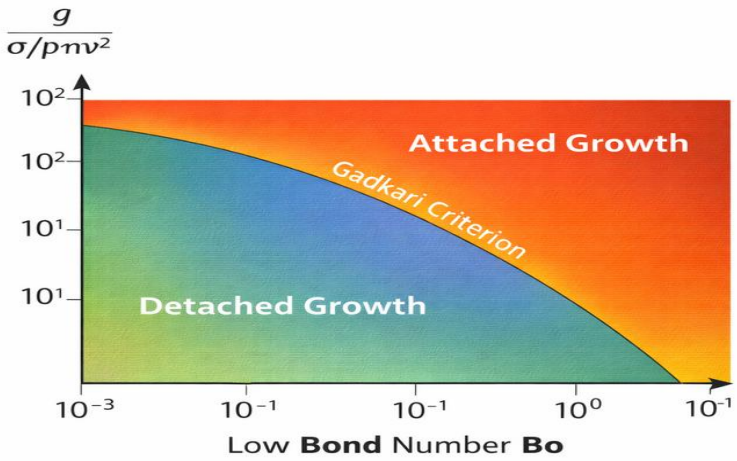

Fig. 6 Experimental observation of crystal-melt interface morphology mapped onto the dimensionless regime map. (a) Concave, capillary-stabilized interfaces are observed when GD < 1, while, convex interface making at end. (b) Gadkari Detached Stability Criterion is line of demarcation of separating the attached, and detached growth regions in the VDS process.

Crystallization Quality and Growth Stability

The detached configuration minimizes:

- wall friction,
- heterogeneous nucleation,
- thermal asymmetry,
- parasitic convection.

Consequently, the crystal grows under near-symmetric thermal and solutal fields, promoting enhanced structural perfection. Similar improvements in crystalline homogeneity were qualitatively indicated in earlier investigations [17–19], while the present results provide direct experimental confirmation through sustained interface stability.

Hence, enhanced crystallization is fundamentally a *process-design outcome*, not a gravity-elimination requirement.

Physical Interpretation

The combined evidence from the present study and references [15–19] supports the following physical picture:

1. Capillary forces establish self-oriented seed
2. Thermocapillary stresses regulate melt flow
3. Convection becomes negligible
4. Interface detaches completely
5. Stable directional crystallization proceeds

Therefore, the governing mechanism is *surface-force dominance under terrestrial gravity*, validating the *Gadkari Detached Stability concept*.

3.4 Mechanism of surface-force-dominated VDS under terrestrial gravity

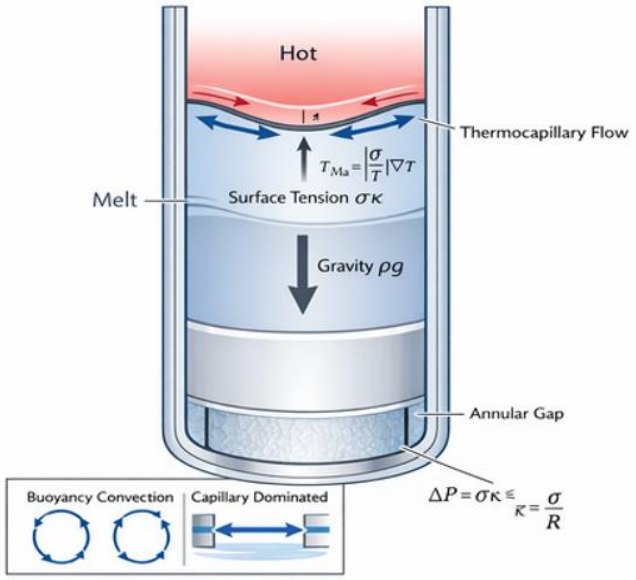

Figure 7. Mechanism of surface-force-dominated VDS under terrestrial gravity. Surface-force-dominated VDS under 1 g. Capillary pressure σκ and thermocapillary shear dominate over gravity (Bo≪1), suppressing buoyancy convection and enabling detached crystal growth (GD≫1

A schematic sealed vertical ampoule (Fig.7) contains the melt between the hot zone (top) and the growing crystal cold zone (bottom) with annular gap. Although a gravitational body force 'ρg' acts downward, the small characteristic radius L and high surface tension σ reduce the Bond number $Bo=\rho g L^2/\sigma \ll 1$, so gravity-driven buoyancy cannot sustain bulk convection. Interface curvature generates capillary pressure ($\Delta P=\sigma\kappa$), while temperature-dependent surface tension produces thermocapillary (Marangoni) shear ($\tau_{Ma}=(d\sigma/dT)\ \nabla T$), which governs melt transport along the meniscus (red arrow). These surface stresses dominate over gravitational stresses (down Big black arrow), suppress hydrostatic wall wetting, and stabilize a curved interface (between white and light black curve lines), resulting in diffusion/thermocapillary-controlled growth and the formation of an annular detached gap. The corresponding stability condition is expressed by the growth-deviation parameter $GD= 1/(Ma+Ca) \gg 1$, indicating a surface-force-dominated (quasi-microgravity) regime.

In conventional terrestrial growth, buoyancy-driven convection arising from density differences (hot (melt-red)–light rise, cold (crystal-light blue)–heavy sink) promotes melt circulation and wall attachment. In contrast, the narrow-gap VDS geometry drastically reduces the Bond number, and capillary/thermocapillary stresses dominate the melt dynamics. Although density gradients remain present, they are unable to generate bulk motion. Consequently, buoyancy transport is suppressed and the system approaches a quasi-microgravity state, enabling detached crystallization.

During VDS under terrestrial 1 g conditions, the melt motion is governed by the incompressible Navier–Stokes equations with buoyancy, capillary, and thermocapillary stresses. Non-dimensionalization introduces the Bond number $Bo=\rho gL^2/\sigma$, which represents the ratio of gravitational to surface-tension forces. Owing to the small ampoule radius and high melt surface energy, $Bo \ll 1$, so the characteristic gravity stress 'ρgL' becomes much smaller than the capillary stress σ/L. Consequently, the buoyancy term in the momentum equation becomes asymptotically negligible and cannot sustain bulk convection, even though gravity remains present. Melt transport is therefore dominated by capillary pressure and Marangoni shear, described by the Capillary and Marangoni numbers (Ca, Ma), leading to the stability condition $GD= 1/(Ma+Ca) \gg 1$. In this surface-force-dominated regime, the interface shape is controlled by curvature and interfacial energy rather than hydrostatic forcing, suppressing wall attachment and enabling diffusion/thermocapillary-controlled, entirely detached growth. Thus, VDS does not eliminate gravity, but dynamically decouples it from the crystal-melt interface solidification front, producing a quasi-microgravity crystallization environment in the asymptotic limit $Bo \to 0$.

The melt dynamics in VDS are determined by the competition between gravitational and interfacial stresses. Scaling of the momentum equation yields the Bond number $Bo=\rho gL^2/\sigma$, which compares gravity with capillarity. For the narrow ampoule geometry used here, $Bo \ll 1$, so the gravity term becomes dynamically negligible. The interface is instead controlled by capillary pressure $\Delta P=\sigma\kappa$ and thermocapillary shear $\tau_{Ma}=(d\sigma/dT)\,\nabla T$, leading to surface-driven flow rather than buoyancy convection. Under these conditions, melt transport becomes diffusion/thermocapillary dominated, suppressing wall attachment and enabling entirely detached crystal growth. This behavior corresponds to the stability limit $GD \gg 1$, where surface forces outweigh gravity and the system approaches a quasi-microgravity solidification environment.

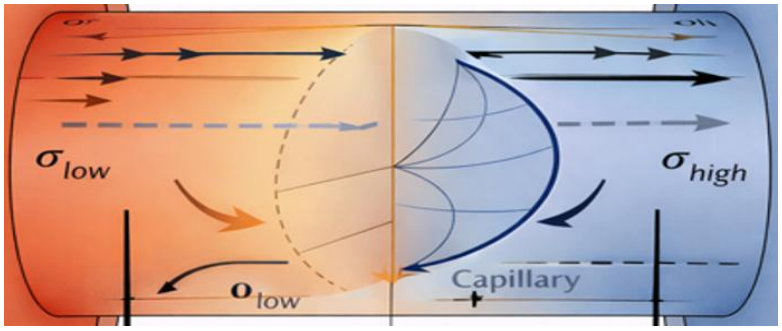

Figure 8. Capillary–thermocapillary coupling inside the vertically oriented VDS ampoule, in between hot and blue colour is a gap width (entirely detachment)), following the standard temperature convention (blue: cold crystal zone, orange: intermediate melt, red: ampoule inner wall hot zone). The axial temperature gradient establishes a surface-tension gradient that drives Marangoni flow along the annular melt film toward the interface-melt solidification front, while curvature-induced capillary pressure sustains inward liquid suction and prevents wall wetting. Gravity acts downward (vertical two bold blue lines at left and right) but remains weak in the thin-film regime. The combined

surface forces maintain a stable melt ring and enable entirely detached crystal growth under terrestrial conditions.

The *complete force balance and transport physics* occurring in the annular melt gap of the VDS process in Figure 6. The temperature field varies only *axially* (not radially or side-to-side), consistent with vertical furnace operation:

- Crystal → cold → blue
- middle → intermediate melt → orange
- Melt at top → hot source → red

Because surface tension decreases with increasing in temperature,

$\sigma_{(T)}=\sigma_0+d\sigma/dT(T-T0)$, $d\sigma/dT<0$

the hot melt exhibits lower surface tension and the colder interface higher surface tension. This produces

$\nabla\sigma=|d\sigma/dT|\nabla T$,

which generates thermocapillary shear $\tau_{tc}=\nabla\sigma$

and drives Marangoni transport toward the growth interface. Simultaneously, the curved meniscus inside the thin annulus creates Young–Laplace suction,

$\Delta Pc\sim\sigma h$

feeding melt into the gap and preventing crystal–wall contact. Since

$Bo=\rho gh^2/\sigma\ll1$,

Gravity-induced force is negligible compared with surface forces. These coupled mechanisms provide the physical basis for the *Gadkari Detached Stability Criterion* and explain sustained entirely detached growth in 1 g.

Meaning of arrows in Figures, Solid horizontal arrows along the interface

→ Marangoni (thermocapillary): Flow direction (Melt motion from low-σ (hot) to high-σ (cold) region. Curved inward arrows near the meniscus/gap

→ Capillary suction (Young–Laplace pressure): Melt drawn into the annular ring to maintain detachment. Circular/recirculating arrows inside the melt

→ Internal convection loops: Redistribution of heat and solute within the thin film. Dashed arrows along the axis (vertical orange line at the centre of figure)

→ Temperature gradient (∇T): Direction of imposed furnace gradient. Downward vertical arrow labelled g (two black vertical lines at left and right)

→ Gravity-induced force/buoyancy direction: Shown for reference; effect small because $Bo\ll1$

- Thermocapillary transport feeds the interface, capillary suction maintains the gap, and gravity-induced force is negligible — together producing entirely detached growth, this is the Physical significance of Figure 6.

Surface-tension gradients generate tangential Marangoni shear that transports melt from the hot region toward the colder crystallization front, continuously replenishing the interface. Simultaneously, curvature of the meniscus within the narrow annulus produces capillary suction that stabilizes the liquid ring and prevents wall wetting. The combined action of these two mechanisms maintains a persistent melt film separating the crystal from the container. Thus, thermocapillary flow provides dynamic feeding, whereas capillary pressure provides static mechanical separation.

4. Discussion Statement

Entirely detached growth in VDS arises when surface forces dominate gravity-induced force (Bo $\ll$ 1, GD $\gg$ 1), suppressing buoyancy-driven convection and eliminating hydrostatic wall contact. Under this condition, the interface is stabilized by capillary pressure ($\Delta P = \sigma\kappa$) and thermocapillary shear, resulting in diffusion-controlled, symmetric solidification. The absence of mechanical and thermal disturbances minimizes lattice strain and defect formation. Consequently, XRD shows reduced peak broadening and lower 2θ, Table-4, Laue patterns exhibit sharp and symmetric reflections, FTIR reveals smooth band-gap variation indicating chemical homogeneity, and Hall measurements demonstrate improved carrier transport Fig- 5. Microhardness, EPD, and Raman spectra attributed to improved crystallinity of the Sb-based materials by VDS process. These combined signatures confirm that surface-force-dominated detached VDS directly enhances crystallization quality.

The present experiments, together with our earlier systematic studies [25-48], conclusively demonstrate that entirely detached and stable crystal growth in VDS Solidification is achievable under 1g when the Bond, Capillary, and Gravity deviation numbers are simultaneously minimized through appropriate ampoule geometry and thermal control. These findings establish that enhanced crystallization is fundamentally governed by capillary–thermocapillary physics rather than by microgravity conditions alone.

This study establishes that enhanced crystallization under terrestrial gravity (1g) is not fundamentally constrained by gravity itself, but is predominantly governed by process architecture and ampoule geometry; when these parameters are optimally engineered, the resulting solidification dynamics and crystal quality can match those typically achieved under space-based or microgravity conditions.”

The findings indicate that enhanced crystallization under terrestrial gravity (1g) is strongly influenced by process design and ampoule geometry; appropriate control of these parameters enables growth regulation approaching the stability and crystal quality reported for space-based or microgravity conditions.

Conclusion

The present study provides direct experimental evidence that entirely detached crystal growth can be achieved and sustained during VDS under terrestrial gravity through appropriate

geometric and thermal design of the ampoule. Sequential observations demonstrate spontaneous self-oriented seeding at the conical bottom, followed by progressive interface separation and eventual formation of a continuous annular gap along the full circumference of the crystal–melt. Measurements of the detachment gap, stability duration, and interface planarity confirm that the detached configuration remains steady throughout growth, without wall wetting or intermittent reattachment. The calculated nondimensional parameters show consistently low Bond ($Bo \ll 1$), Capillary ($Ca \ll 1$), and Growth deviation ($GD \ll 1$) numbers, establishing that capillary and thermocapillary stresses exceed buoyancy forces. Under these conditions, the interface curvature-induced pressure stabilizes the front, suppresses convection, and produces symmetric heat and mass transport, resulting in uniform ingot morphology and improved crystallization quality.

These findings extend our earlier experimental investigations, where only partial or transient detachment was observed. In contrast, the present configuration achieves fully reproducible and entirely detached growth across multiple runs, demonstrating that interface stability is governed primarily by process design and ampoule geometry rather than by external gravity reduction. The results therefore validate the detached growth regime predicted by the *Gadkari Detached Stability Criterion* concept and establish a quantitatively surface-force-dominated solidification mechanism.

Importantly, the observed behavior closely replicates characteristics commonly reported in microgravity crystal growth, including planar interfaces, minimized melt convection, and reduced wall interaction. However, the present experiments demonstrate that such microgravity-like stability can be reproduced under normal 1g conditions by minimizing Bo, Ca, and GD through geometric confinement and controlled thermal gradients. Thus, gravitational decoupling is achieved physically rather than environmentally, eliminating the need for space-based processing to obtain stable directional crystallization.

In VDS, the combination of capillary pressure, thermocapillary shear, and geometric confinement reduces the Bond number far below unity. Under this condition, buoyancy-driven convection is mechanically suppressed, and the melt–interface dynamics become governed primarily by surface stresses. Although terrestrial gravity remains present, its influence on growth becomes negligible, resulting in a quasi-microgravity crystallization environment.

Although terrestrial gravity is present during VDS, the combined effects of capillary pressure, thermocapillary shear, and geometric confinement drastically reduce the Bond number. Under these conditions, surface stresses dominate over buoyancy forces and suppress gravity-driven convection. Consequently, melt transport becomes diffusion/thermocapillary controlled, the interface shape is governed by surface energy, and crystal growth proceeds in a quasi-microgravity environment, enabling stable and entirely detached crystallization.

Looking forward, the VDS approach offers significant scientific and technological potential. The demonstrated capillary-controlled regime provides a pathway for scalable terrestrial growth of high-quality semiconductor and compound crystals, improved defect suppression, and predictable interface control. Future work may focus on quantitative optimization of ampoule dimensions, adaptive thermal gradients, in-situ interface monitoring,

and extension of the methodology to multicomponent and low-surface-tension systems. These developments can broaden the applicability of VDS alike microgravity processing for advanced crystal growth and materials manufacturing.

Acknowledgement

The author acknowledges the experimental facilities and technical support that enabled the Vertical Directional Solidification (VDS) crystal growth experiments reported in this work. The author also acknowledges long-term research efforts and experimental developments that contributed to establishing entirely detached growth under terrestrial conditions. The author expresses sincere gratitude to Prof. B. M. Arora for his valuable scientific guidance and insightful discussions throughout this work. The author also thanks Dr. Shilpa Kalantre for continuous encouragement, Ms. Snehal Gadkari for computational support, and Mrs. Sarojini Gadkari for her unwavering motivation.

Author Contributions: Dattatray Gadkari conceived the study, designed the experiments, performed the crystal growth runs, analyzed the data, developed the theoretical framework, prepared all figures and tables, and wrote the manuscript.

Data Availability Statement: The experimental data, measurements, and supporting materials generated during this study are inserted into this manuscript

Competing Interests: The author declares that there are no competing financial or non-financial interests related to this work.

Ethical Approval: This study does not involve human participants or animals. Therefore, ethical approval is not required.

References

1. Wang, Y., Regel, L. L., Wilcox, W. R. J. Cryst. Growth (2000) 209, 175.
2. Wang, Y., Regel, L. L., Wilcox, W. R. (2002) J. Cryst. Growth 243, 546.
3. Wang, J. B., Regel, L. L., Wilcox, W. R. J. Cryst. Growth 2(2004) 60, 590.
4. Yeckel, A., Derby, J. J. J. Cryst. Growth (2009) 311, 2572.
5. Yeckel, A., Derby, J. J. J. Cryst. Growth (2011) 314, 310.
6. Duffar, T. et al. J. Cryst. Growth (2000) 211, 434.
7. Duffar, T. et al. J. Cryst. Growth (2001) 223, 69.
8. Balint, S. et al. J. Cryst. Growth (2008) 310, 1564.
9. Hayakawa, Y. et al. Int. J. Microgravity Sci. Appl. (2017) 34, 340111.
10. Yu, J. et al. npj Microgravity (2019) 5, 1.
11. Jin, X., Wang, B. J. Cryst. Growth (2023) 607, 127110.
12. Ghritli, R., Okano, Y., Dost, S. J. Cryst. Growth (2021) 573, 26280.

13. Ghritli, R., Okano, Y., Dost, S. Jpn. J. Appl. Phys. (202261, 115502.
14. Costesèque, P., Mojtabi, A., Platten, J. K. C. R. Mécanique (2011) 339, 275.
15. Rahman, M. A., Saghir, M. Z. Int. J. Heat Mass Transfer (2014) 73, 693.
16. Eslamian, M., Saghir, M. Z. Int. J. Therm. Sci. (2011) 50, 1232.
17. Alexandrov, D. V., Aseev, D. L. Comput. Mater. Sci. 37 (2006) 1.
18. Chen, M. W. et al. J. Cryst. Growth (2022) 590, 126703.
19. Krüger, A. T. et al. Phys. Rev. B (2023) 107, 064301.
20. Stelian, C., Yeckel, A., Derby, J. J. J. Cryst. Growth (2009) 311, 2572.
21. Rudolph, P. AIP Conf. Proc. (2010) 1270, 107
22. Rudolph, P., Czupalla, M., Lux, B. J. Cryst. Growth (2009) 311, 4543.
23. Bright et al., J. Heat Transfer (2014) 136, 062701.
24. Liu, X., Fan, H., Shan, Y. PLoS ONE (2024) 19, e0313150
25. Gadkari D. B., Lal K. B., Arora B. M., Proc. DAE Solid State Physics Symp India, (1994) 37 C, 198, abid (1995) 38C, 72
26. Gadkari D. B., Lal, K. B., Arora B. M., (Rapid Communication) J. Crys Growth (1997) 175, 585
27. Gadkari D. B., Lal K. B., Arora B. M., Bull. Mater. Sci. (1998) 21, 127.
28. Gadkari D. B., Lal K. B., Arora, B. M., Indian Patent 139/BOM/1999 (1999) and (2004)192132
29. Gadkari D. B., Lal K. B., Arora B. M., Indian J Pure Applied Phys (1999) 37, 65
30. Gadkari D. B., Arora B. M., Indian J Pure & Applied Physics (2000) 38, 237
31. Gadkari D. B., Lal K. B., Arora B. M., Bull. Mater. Sci. (2001) 24, 475
32. Gadkari D. B., Arora B. M., Transaction Materials Soc Japan (2009) 34, 571
33. Gadkari D.B., J Chemi Chemi Engin (2012) 6, 65
34. Gadkari D.B., J Chemi Chemi Enginee (2012) 6, 250
35. Gadkari Dattatray, J Materi Sci Engin (2012) A2, 9, 593
36. Gadkari D. B., AIP Conf. Proc. (2013) 15, 12 856. http://dx.doi.org/10.1063/1.4791308
37. Gadkari D.B., J Materi Sci Engineeg (2013) A3 5, 338
38. Gadkari D.B., Arora B.M., Mate Chemi Phys (2013) 139, 375, https://doi.org/10.1016/j.matchemphys.2012.09.060
39. Gadkari D. B., Interna J. Sci Res Publ (2014) 4, 01

40. Gadkari Dattatray, Doped InSb Detached Crystals by VDS Technique: Its Substrates for Infrared Devices and Physics Concept. Intern J Enginee Appl Sci (IJEAS) (2015) 2, 39

41. Gadkari Dattatray, Dilip Maske, M. Deshpande, Brij Mohan Arora, IJIRSET (2016) 5, 20925, doi:10.15680/IJIRSET.2016.0502059 2092

42. Gadkari D. B., Int. J Engin Resea. Appli. (2019) 9, 01

43. Gadkari D B, Int J Eng Res App (2020) 10, 5

44. Gadkari D B, Int J Eng Res App (2020) 10, 35

45. Gadkari D B, Int J Eng Res App (2020) 10, 07

46. Gadkari, Dattatray B., Intern J Engin Res Appli, (2025) 11, 121-132. www.ijera.com

47. Gadkari Dattatray, International Journal of Science and Technology, (2026) 17(1). DOI: https://doi.org/10.71097/IJSAT.v17.i1.10166

48. Gadkari Dattatray, International Journal of Science and Technology, (2026) 17(1). DOI: https://doi.org/10.71097/IJSAT.v17.i1.10260